

Airborne Magnetic Anomaly Navigation

AARON CANCIANI

JOHN RAQUET

Air Force Institute of Technology, Fairborn, OH, USA

Robust aerial navigation without GPS is a challenging problem. Alternative navigation systems for airborne use are often limited by where and when they can operate. For example, terrain following systems cannot operate over oceans, and star-tracker and computer-vision systems depend on weather and daylight. Navigation using the Earth's magnetic anomaly field, which is globally available at all times, shows promise to overcome many of these limitations. We designed an airborne navigation system that utilizes only passive instruments—an optically pumped scalar magnetometer, an inertial navigation system (INS), a barometer, and a magnetic anomaly map. The navigation system uses a particle filter to correct errors in an INS as well as estimate measurement-corrupting temporal variations by comparing actual magnetometer measurements to expected measurements from the magnetic anomaly map. A complete measurement equation is presented that describes the nontrivial relationship between the real-time magnetometer measurements and the magnetic anomaly map. We validated the navigation system with real data from a flight test over Louisa, VA. Horizontal DRMS errors of 13 m were achieved over an hour long flight at the map altitude of 1000-ft MSL using a magnetic anomaly map created 3 years ago. This result should be considered as a “best case” result when using the presented methods, since the flight test was conducted in ideal conditions. The demonstrated accuracy of the navigation system shows orders of magnitude improvement over previously published magnetic navigation experimental results, indicating that the magnetic anomaly navigation is a promising addition to current global positioning system alternative and backup systems.

Manuscript received September 10, 2015; revised June 20, 2016; released for publication July 13, 2016. Date of publication January 9, 2017; date of current version April 17, 2017.

DOI. No. 10.1109/TAES.2017.2649238

Refereeing of this contribution was handled by J. Morton.

Authors' addresses: The authors are with the Autonomy and Navigation Technology Center, Air Force Institute of Technology, Fairborn, OH 45324 USA, E-mail: (aaron.canciani@afit.edu).

This paper has supplementary downloadable material available at <http://ieeexplore.ieee.org>.

0018-9251 © 2017 IEEE

I. INTRODUCTION

Navigation using the Earth's magnetic anomaly field holds strong potential as a global positioning system (GPS) alternative. Using environmental signals for navigation has been widely studied. Vision-based systems, gravity gradiometry, and terrain following navigation systems are all potential navigation signals that lead to various degrees of navigation accuracy [1]–[3]. Absolute positioning using magnetic fields has been used for indoor and ground-based navigation, but this paper focuses on the benefits and challenges of the airborne case [4], [5].

Using a magnetic anomaly map for navigation has several advantages over alternative navigation systems. Terrain and vision systems can only operate over the one-third of the Earth covered by land. Terrain systems do not work well over flat land such as deserts, and vision systems degrade over areas with limited features like forests. The Earth's magnetic anomaly field varies over oceans, forests, and deserts, providing a signal where other alternative systems fall short. Furthermore, magnetic anomaly navigation is not dependent on weather or time of day. Finally, magnetic anomaly navigation is completely passive and difficult to corrupt, either intentionally or unintentionally, because the measured magnetic field decays much faster with distance from a source than an RF signal. Jamming a magnetometer on an aircraft would require far more energy than a radio-based navigation system.

One of the largest benefits of using magnetic anomaly fields for navigation is the ability to use a continuous map. A magnetic anomaly field can be fully sampled according to the Nyquist sampling criteria. In aeromagnetic surveys, the sample spacing needed to fully sample the signal is approximately equal to the height above terrain [6]. Having a fully sampled magnetic field map allows for accurate interpolation between grid points. This creates a subtle but important difference between similar terrain-based navigation systems. Small terrain variations like trees and buildings are likely not captured in a terrain map and will corrupt a terrain height measurement [7]. A magnetic anomaly map, which is sufficiently sampled, can be guaranteed to capture the entire magnetic anomaly field. This allows for very small measurement uncertainties that help to reject other corrupting fields from a magnetometer measurement, such as space-weather and aircraft sources.

A magnetic anomaly map is the difference between the scalar magnetic field magnitude at any point in space and the predicted magnetic field from a reference model. This reference field is a long-wavelength Earth magnetic field model, such as the international geomagnetic reference field (IGRF) [8]. The magnetic field at any point in space is the summation of all magnetic sources. The major sources include the Earth's core field, the crustal field, and the temporal variations (ionospheric and magnetosphere fields) [9]. Care is taken to remove temporal variations when creating magnetic anomaly maps so they, therefore, primarily reflect the Earth's crustal field. The physical significance of magnetic anomaly maps is subtle—because

the Earth's core field is so much larger than the crustal field, the scalar subtraction of the measured field and the core field, which are both vector fields, approximates the magnetic anomaly field projected in the direction of the main Earth field. This is because small vector anomalies perpendicular to the main Earth field vector will not change the overall vector length by a noticeable amount. Consequently, only crustal sources which "stretch" or "shrink" the main Earth field vector (by being parallel or antiparallel) can significantly change the magnetic anomaly map value. See [10] for a more complete description of the components of the Earth's magnetic field with respect to navigation. By removing the time-varying core field as well as the temporal variations, a magnetic anomaly map represents a nontime-varying field. A magnetic anomaly map is, therefore, a suitable candidate for navigation.

There are several key difficulties with magnetic anomaly navigation that must be overcome to achieve the accuracy demonstrated in this paper. The first is the need for a high-quality magnetic anomaly maps. The Earth's magnetic field varies in three dimensions and consequently the field at aircraft altitudes cannot be measured by satellites. Magnetic anomaly maps are generally created by geosurvey companies flying aircraft at low altitudes over the area of interest. These maps are created at varying resolutions, and may be fully-sampled as described previously. Under-sampled maps will degrade navigation performance. Almost all modern magnetic anomaly maps are created with the use of the GPS to geo-reference data. However, many large compilation magnetic anomaly maps, such as the North American magnetic anomaly database [11], are created from individual maps that were made before the use of GPS. Consequently, these maps are less accurate than modern maps created with GPS. This indicates that these continent and world sized maps will not achieve the same level of accuracy as a post-GPS era magnetic anomaly maps.

Platform motion is required to achieve accurate magnetic anomaly navigation. A single-magnetometer measurement alone can only constrain a position solution to a contour line along the magnetic anomaly map (a line of constant magnetic intensity). It is the unique changes in the magnetic field along a given trajectory that lead to full observability of the platform position. The high-dynamic motion of the platform during our flight test is one of the reasons the presented results are considered "best-case."

Another obstacle to accurate magnetic anomaly navigation is an altitude dependency. The frequency content of the Earth's magnetic anomaly field decreases with altitude [12]. Increasing altitude essentially acts as a low-pass filter on the magnetic anomaly map. This low-pass filtering of the data means that the gradient of the magnetic field is decreased, which directly effects navigation accuracy in similar systems [13]. Consequently, the highest accuracies in magnetic anomaly navigation will be achieved at lower altitudes. It is important to note in this context that "altitude" refers to altitude above terrain. Increasing altitude above terrain is what leads to decreased frequency content in the field. This

indicates that when flying over an ocean, the altitude above terrain will be equal to the altitude above sea level plus the ocean depth. Flying at 1 km above sea level over 1-km deep ocean should lead to similar navigation accuracies as flying at 2-km altitude over land. Finally, calibration is a major concern for accurate magnetic anomaly navigation. The results achieved in this paper used a magnetometer on a boom. A magnetometer inside an aircraft would require additional calibration to remove aircraft fields. The feasibility of this calibration and the navigation accuracy possible using a magnetometer inside an aircraft has not yet been studied.

There are few published experimental results on magnetic anomaly navigation. Some of the first research was completed by the Naval Command, Control and Surveillance Center with submarines in the late 1980's [14]. The navigation techniques showed promise but position errors were quite large, on the order of many kilometers. Satellite positioning was explored with magnetic fields described in [15], with position accuracies on the order of tens of kilometers. The Earth's magnetic field contains much more variation at lower altitudes, suggesting magnetic navigation may be more accurate at lower altitudes. Airborne navigation was attempted with flux-gate magnetometers described in [16] with obtained accuracies on the order of kilometers at low altitudes. Flux-gate magnetometers are orders of magnitude less accurate than optically-pumped scalar magnetometers, suggesting better performance may be possible with optically-pumped magnetometers. These magnetometers are used in geological surveys and have an accuracy of better than 1 nT [17]. Even if high-quality vector magnetometers were available, the vast majority of existing magnetic maps are created with scalar sensors. This indicates an improved vector sensor would require large amounts of re-mapping. Also, a vector sensor measurement will always be limited by the knowledge of aircraft attitude. A vector measurement made in the body frame would need to be rotated into a navigation frame to be useful in a map-based system. Any errors in aircraft attitude would manifest as measurement errors when resolving the vector measurement. Several authors have discussed algorithmic implementation of magnetic anomaly navigation, treating it as closely related to terrain-based navigation, and present simulation-only results [18]–[20]. Treating magnetic anomaly navigation as simply analogous to terrain-based systems ignores important considerations that will lead to decreased navigation accuracy. For example, the majority of the papers ignore the crucial fact that the magnetic anomaly field varies in three dimensions and often neglect space weather effects as well as aircraft fields. These issues are addressed in this paper. A theoretical discussion of geomagnetic navigation with flux-gate instruments is given in [21], although no experimental or simulated results are given.

There are a large variety of target applications for magnetic anomaly navigation. As discussed previously, magnetic anomaly navigation works well where other alternative navigation systems fall short, such as oceans, deserts, and forests. Magnetic anomaly navigation also seems

promising for low flying UAV applications, such as agriculture. The high spatial variations in the magnetic anomaly field seen at low altitudes can lead to high accuracy navigation. The cost of an optically pumped magnetometer, of the type used in this research, costs between \$15 000 and \$25 000. The instrument itself is a cylinder of about 2 in in diameter and 5 in long. The cost of this instrument as well as the size may somewhat limit the application to larger UAV's or full-size aircraft.

This paper applies an approach to magnetic anomaly navigation, which we initially described in [10], to data from a real flight. In [10], we presented a particle-filter-based approach to magnetic anomaly navigation in which measurements from a magnetometer were compared to a magnetic anomaly map to correct errors in an inertial navigation system (INS). We showed that the temporal variations were a dominant error source and included them in the filter model. We showed that the filter had observability of the low-frequency components of the temporal variations. In this paper, we apply a slightly modified filter to real instrument data obtained from a test flight conducted by the geo-survey company Sander Geophysics. The rest of this paper is organized as follows. Section II presents the full measurement equation for magnetic anomaly navigation. Section III presents the filter design, and Section IV presents the results of applying the filter to the real flight data. Section V presents our conclusions and the Appendix describes the full navigation algorithm necessary to implement the designed marginalized particle filter (MPF).

II. MEASURING THE MAGNETIC ANOMALY

Defining the measurement equation for magnetic anomaly navigation is an important and first step in designing an estimation filter. The measurement equation describes how the raw measurements from a magnetometer relate back to the filter states. An intermediate goal is to determine how the raw measurements relate back to a magnetic anomaly map. The individual errors present in the raw magnetometer measurement are presented below.

A. Map Quality

Map quality is a significant factor in magnetic anomaly navigation. Many magnetic anomaly maps were created before the use of GPS. The magnetometer data, therefore, may not be geo-located as accurately as modern magnetic surveys. A map created without the use of GPS will possibly lead to degraded navigation performance. If using a magnetic anomaly map that was made without the use of GPS, a navigation filter would likely need to have a greater measurement error covariance. In general, it is suspected that the highest accuracy navigation will be obtained with recent magnetic anomaly maps. Map resolution is also an important concern. As stated previously, a magnetic survey must be flown with sample spacing no greater than the height above the terrain to fully sample the field. Not all magnetic anomaly maps meet this criteria. These maps will therefore have uncaptured high-frequency components that will lead

to degraded navigation performance. Finally, many magnetic anomaly maps are created at a “drape” altitude. These maps are flown at a constant height above terrain rather than a constant barometric height. Fortunately, these maps can be upward continued to a constant barometric height. This process requires the original drape altitude that was flown, however, and this may not always be available. Treating a draped map as a constant elevation map will lead to decreased navigation performance.

B. Altitude Dependent Variations

Navigation accuracy is dependent on altitude. The Earth's magnetic anomaly field exists in three dimensions. As altitude increases, the spatial-frequency content of the signal decreases. This decreased spatial-variation in the field degrades navigation performance. Navigation at aircraft altitudes has the benefit of being far closer to the magnetic sources than navigation at satellite altitudes, and consequently can achieve much better accuracy. Magnetic anomaly maps are only flown at one altitude—usually very low. As described in [10], we can upward continue this data. This process is error prone, however, especially with a small map, due to edge effects. The need for upward continuation can be ignored if flying at the survey altitude; however, this is certainly not feasible for all or even most aircraft missions. If flying at an altitude below a magnetic anomaly map, a upward continuation line filter can be applied to help the measurements match the higher altitude magnetic anomaly map. This is preferred to downward continuing the map tile because downward continuation is unstable and leads to nonunique solutions, whereas upward continuation is stable. This navigation results will not be as accurate as they would have been had a lower altitude map been available, as some of the high-frequency content in the measurement is being thrown out.

C. Corrupting Sources

A magnetometer mounted on an aircraft measures the total magnetic field. We are attempting to use a distinct component of this field for navigation, the crustal field. The other three components of the total field can be thought of as measurement errors, or corrupting sources. The total measurement includes four main components:

- 1) main Earth field;
- 2) aircraft field;
- 3) temporal variations (ionospheric and magnetospheric sources); and
- 4) crustal field.

The measurement equation must include all four of these terms. The main Earth field is the easiest of the three corrupting fields to remove. The main Earth field is well modeled by the IGRF, a freely available model that is easy to evaluate for a given latitude, longitude, altitude, and time [8]. The IGRF field changes so slowly with respect to location that only a rough position estimate must be known to subtract out this field. The aircraft field is mostly

removable. Modern aircraft compensation systems can remove the aircraft field to fractions of a nano-Tesla [8]. Aircraft compensation systems use a short segment of training data to calibrate out the majority of the aircraft effects. These training data are obtained by flying at a high altitude (> 3 km) over an area of low magnetic anomaly spatial variation. The aircraft flies in a square pattern and performs a series of roll, pitch, and yaw maneuvers along each leg of the square pattern. The measurement data are band-pass filtered to ensure that no magnetic crustal variations appear in the measurements (this is already helped by flying at a high altitude over an area of low magnetic anomaly variability). Any variations seen in the bandpass filtered data can then be attributed to aircraft effects. This data are used along with the aircraft orientation within the magnetic field (obtained by a separate vector magnetometer or an INS) in a simple least-squares batch filter to minimize the observed aircraft effects. Geo-survey companies have real-time compensation systems that can perform these operations automatically [8]. The implementation of one of these compensation systems is beyond the scope of this paper—for our navigation filter, we used the compensated measurements provided by the commercial compensation system the geo-survey company was using. Once an aircraft has been calibrated, the same calibration coefficients can be used in future flights if the aircraft configuration remains the same.

After the removal of the main Earth field using the IGRF and applying aircraft field compensation, the temporal variations are the largest remaining error. “Temporal variations” is the term used to group all space weather effects on the Earth’s magnetic field. As explained fully in [10], these sources are primarily caused by electrical currents in the Earth’s ionosphere and magnetosphere. The main daily variation in the temporal variations is caused by a diurnal effect in the Earth’s ionosphere. Magnetic storms interacting with the Earth’s magnetosphere are responsible for many of the larger variations. If unaccounted for, temporal variations can affect navigation performance. The effect of temporal variations can be mitigated, however. In [10], the observability of real-world temporal variations by a magnetic anomaly navigation filter was shown in a simulation environment. When the filter estimated the temporal variations, the strength of the magnetic storm conditions did not have a large effect on navigation performance. Transmitting the temporal variations from a nearby base station is a feasible but potentially undesirable way to remove the temporal variations.

D. Measurement Equation

In light of the given error sources, we can present the full measurement equation for magnetic anomaly navigation. First, we present the errors in the three-dimensional (3-D) map function to be used by the navigation system. We use the \models symbol to denote “models.” The below expression describes how the 3-D interpolation object is created from upward continuing a 2-D gridded map tile, and describes

what errors are inherent to that process

$$M_3(\text{lat}, \text{lon}, h) \models f_I^3(f_U(M_{h_0} + \delta M_{h_0}) + \delta U) \quad (1)$$

where

M_{h_0}	2-D grid of magnetic intensity values at height h_0 ;
δM_{h_0}	errors in the original map grid;
f_U	upward continuation function that transforms
M_{h_0}	to several discrete increasing altitudes, giving a 3-D grid of values from the original 2-D grid;
δU	error in the upward continuation transform;
f_I^3	operation that returns a 3-D interpolation function given a 3-D grid of values;
lat, lon, h	latitude, longitude, and height, respectively, at which the magnetic intensity is being evaluated;
$M_3(\text{lat}, \text{lon}, h)$	3-D interpolation function that returns expected magnetic intensity at a given latitude, longitude, and altitude.

We found linear interpolation between grid points to be sufficient. This is expected, because we know that the magnetic anomaly map is continuous and fully sampled. Note that having linear interpolation between grid points does *not* mean that the measurement update is linear. To understand this, imagine a perfect measurement update starting with a large initial uncertainty. The measurement update would constrain the navigation solution to an entire contour line on the map (a line of equal magnetic intensity). This type of update is, therefore, nonlinear and nonGaussian. The magnetic anomaly measurement equation for a *postcompensated* measurement can be given by

$$Z_t = M_3(\text{lat}, \text{lon}, h) + I(\text{lat}, \text{lon}, \text{alt}, t) + \delta I(\text{lat}, \text{lon}, \text{alt}, t) + \delta C(\theta, \phi, \psi) + V(\text{lat}, \text{lon}, h, t) + H + b + w \quad (2)$$

where

Z_t	raw measurement from the magnetometer at time t ;
$M_3(\text{lat}, \text{lon}, h)$	precomputed 3-D interpolation function that returns expected magnetic intensity;
I	IGRF magnitude, which depends on both position and time;
δI	error in the IGRF magnitude, which depends on both position and time;
θ, ϕ, ψ	aircraft Euler angles;
δC	residual aircraft field after compensation as a function of attitude (given by Euler angles);
V	temporal variation, which is a function of both position and time;
$H(\theta, \phi, \psi)$	magnetometer heading error, which is a function of aircraft attitude [22];
b	time-correlated magnetometer bias;
w	magnetometer white noise.

This measurement equation is intentionally as general as possible—simplifications can likely be made depending on the specific circumstances of the flight. We will end this section by presenting the ideal situation for a magnetic anomaly navigation system. Assume a high-quality magnetic anomaly map exists over the area in which we want to fly. Assume we wish to navigate over this map at the survey altitude h_0 . These two assumptions allow us to avoid using upward continuation. We, therefore, create an interpolation function directly out of the 2-D grid and call it M_2 . Furthermore, assume we are flying in an aircraft ideally suited for magnetic anomaly navigation, such as a geo-survey aircraft. The compensation systems of these aircraft routinely remove the aircraft field to a fraction of a nano-Tesla, so we will drop the δC term. The δI term, which represents the errors in the IGRF field, will be assumed constant, and will be grouped in with the temporal variations V . This is a reasonable assumption, as the core field is a long wave-length model. Measurement accuracy in our context is not the same as sensor accuracy—our ability to remove the aircraft fields and temporal variations are what really drive measurement accuracy. Because of this, we neglect two sensor errors, the heading error H , and sensor bias b terms. These sensor errors are quite small compared to the aircraft effects and temporal variations—less than 1 nT. These errors will never be observable in our navigation system and they are small so we do not attempt to model them. The final sensor error is the magnetometer white noise w , which has a variance of q . Under the ideal case presented, our measurement equation simplifies to

$$Z_t = M_2(\text{lat}, \text{lon}) + I(\text{lat}, \text{lon}, \text{alt}, t) + V(\text{lat}, \text{lon}, h, t) + \hat{w}. \quad (3)$$

We wish to relate the measurement to an aircraft's latitude and longitude. Removing the I term is trivial—the IGRF model is simply evaluated at the estimated position. As stated previously, this is a long wave length model and an approximate location will suffice (any errors will likely be constant offsets). This leaves the V term as the only remaining nonwhite error in the measurement equation. We could make another assumption that we have a base station transmitting the temporal variations to the aircraft, but this may be impractical from an operational standpoint. We could also group the temporal variations (V term) in with the white noise term, although this would greatly increase the noise strength of \hat{w} , and calling the resulting noise source Gaussian is a poor assumption. In [10], an alternative method to handle V was presented—it is added as an observable filter state. With the simplifications made, the measurement relates to an aircraft's latitude and longitude primarily through a highly nonlinear function $M_2(\text{lat}, \text{lon})$ plus a linear term V . We will apply a MPF in the next section to estimate the aircraft's latitude and longitude.

III. FILTER DESIGN

We will now present our filter design for magnetic anomaly navigation. Map-based navigation systems can lead to highly non-Gaussian posterior distributions. A

measurement update from a map can often be multimodal, with a probability distribution reflecting multiple possible locations on a map. We chose to use a particle filter to handle these non-Gaussian distributions. Specifically, we are applying a MPF, also known as a Rao–Blackwellized particle filter [23]. The MPF allows a filter to use particles to represent nonlinear or non-Gaussian states and a Kalman filter (or extended Kalman filter) to represent the linear or linearized states. We wish to model an INS, which will require a high number of filter states. Particle filters are known to handle high-dimensional problems poorly [23]. The MPF uses particles to represent only the nonlinear or non-Gaussian position states. The common description of a MPF describes partitioning the filter states into “linear and nonlinear” states. This can cause confusion in our case because the dynamics of all of our states are linear, as they are based on a linearized INS model. “Nonlinear” in our context refers to the fact that the measurement model, which relates the magnetometer measurements to the position states, is highly nonlinear, and leads to non-Gaussian posterior distributions in the position states. We use particles to model these non-Gaussian posterior distributions in the position states. The linearized model of the nonlinear INS dynamics, described below, is sufficient when using a navigation grade INS—linearization errors are dwarfed by the other error sources. Even when using a lower quality INS, corrective feedback to the INS can keep these linearization errors small. Our filter will consist of a nine-state Pinson INS error model from [24] which contains estimates of the INS position, velocity, and tilt errors, as well as two barometer states, a temporal variation state as described in [10], and a constant offset state.

The temporal variation state is intended to capture the space weather effects, also known as temporal variations, which are corrupting the measurements. As described in [10], the temporal variations can be well modeled by a first order Gauss–Markov random process. Based on an analysis of a years-worth of data, these temporal variations vary by tens of nano-Tesla's over an average day. We demonstrated in [10] that a navigation filter using crustal magnetic anomaly measurements had observability of these temporal variations. This is due to the fact that when flying at aircraft velocities and altitudes, the signal from the crustal field contains higher frequency variations than the temporal variations. This lets the long-wavelength temporal variations be estimated by the navigation filter. There will always be overlapping frequency content from the temporal variations and the magnetic anomaly field. However, the amplitude of the temporal variations decreases with frequency, so the unobservable portions of the temporal variations tend to be small enough to neglect. The overlapping frequencies from the temporal variations and crustal field are directly related to the aircraft altitude and velocity. Flying higher decreases crustal spatial frequencies, and flying slower makes these spatial frequencies manifest as lower time frequencies. This indicates that flying higher and slower will decrease observability of the temporal variations. Simulations have shown that even when flying at 10-km altitude there is still greater signal power in the

crustal variations; however, a filter would probably need to be tuned to give less confidence to the measurement update to account for the increased unobservable temporal variations that would be corrupting the measurements. This also indicates that the proposed method to remove temporal variations may not work well on very slow vehicles, such as boats or submarines. Modeling the temporal variations as a first order Gauss–Markov random process requires two parameters, a time constant and a variance. From empirical analysis of temporal variation data, we choose to model the temporal variations as having a variance of 25 nT and a time constant of 5 min. Testing has shown little sensitivity to the exact values of these parameters.

An inertial navigation system is unstable in the vertical channel and will quickly diverge without altitude aiding. We apply altitude aiding directly to the mechanization equations to constrain the vertical channel. This barometer aiding in the mechanization equations is modeled with the two barometer states. For the constant offset state c , recall that part of forming the measurement equation involves subtracting the IGRF—if an accurate location is not known when the magnetic navigation system is initialized, subtracting the IGRF with an approximate location will lead to a bias. The IGRF is a long-wavelength model so we can assume this bias is constant. It is important to distinguish this constant bias from the temporal variation bias. The temporal variation bias is designed to capture small drifts in the field. If the errors in subtracting the IGRF field led to a large offset, the temporal variation state would not model this well. This gives a total of 13 states that are given as

$$\mathbf{x} = [\delta\text{lat } \delta\text{lon } \delta\text{alt } \delta v_n \delta v_e \delta v_d \epsilon_x \epsilon_y \epsilon_z \delta h_a \delta \hat{a} V c]^T \quad (4)$$

where

$\delta\text{lat}, \delta\text{lon}, \text{ and } \delta\text{alt}$	INS position errors;
$\delta v_n, \delta v_e, \text{ and } \delta v_d$	INS velocity errors;
$\epsilon_x, \epsilon_y, \text{ and } \epsilon_z$	INS tilt errors;
δh_a	aiding altitude error;
$\delta \hat{a}$	vertical acceleration error;
V	filter estimated temporal variation;
c	filter estimated constant bias error.

To implement an MPF, we next have to partition the states into nonlinear and linear components. See [23] for a complete description of the MPF. The two horizontal position states are nonlinear and the remaining states are linear

$$\mathbf{x}_t = \begin{bmatrix} \mathbf{x}_t^n \\ \mathbf{x}_t^l \end{bmatrix}. \quad (5)$$

Eq. (4) is already partitioned correctly. We now express the linear and nonlinear states as a sum of a nonlinear part as well as a linear part, as shown in [23]

$$\begin{aligned} \dot{\mathbf{x}}^n &= f_t^n(\mathbf{x}_t^n) + \mathbf{A}_{n,t}^n(\mathbf{x}_t^n)\mathbf{x}_t^l + \mathbf{v}^n \\ \dot{\mathbf{x}}^l &= f_t^l(\mathbf{x}_t^n) + \mathbf{A}_{l,t}^l(\mathbf{x}_t^n)\mathbf{x}_t^l + \mathbf{v}^l. \end{aligned} \quad (6)$$

The horizontal position states are considered nonlinear states because their posterior distributions (distributions after a map-matching update) are potentially multimodal,

non-Gaussian distributions. The horizontal position state dynamics, however, are still linear. This means there are no nonlinear functions in (6). We can, therefore, simplify (6) by replacing the nonlinear functions f^n and f^l with matrices

$$\begin{aligned} \dot{\mathbf{x}}^n &= \mathbf{A}_{n,t}^n(\mathbf{x}_t^n)\mathbf{x}_t^n + \mathbf{A}_{l,t}^n(\mathbf{x}_t^n)\mathbf{x}_t^l + \mathbf{v}^n \\ \dot{\mathbf{x}}^l &= \mathbf{A}_{n,t}^l(\mathbf{x}_t^n)\mathbf{x}_t^n + \mathbf{A}_{l,t}^l(\mathbf{x}_t^n)\mathbf{x}_t^l + \mathbf{v}^l. \end{aligned} \quad (7)$$

It is helpful to think of these matrices as follows:

- \mathbf{A}_n^n represents how the nonlinear states propagate with respect to themselves;
- \mathbf{A}_l^n represents how the nonlinear states propagate with respect to the linear states;
- \mathbf{A}_n^l represents how the linear states propagate with respect to the nonlinear states;
- \mathbf{A}_l^l represents how the linear states propagate with respect to themselves.

Each of these four matrices is needed in the equations for the MPF. These four matrices are simply the INS Pinson error model (see [24]) partitioned into four components, with the addition of the barometer, temporal variation, and constant offset states. Latitude and velocity appears in several terms of the dynamics matrices. When these values are needed we use the filter corrected values of these states, rather than the uncorrected INS values. These four matrices are given by

$$\mathbf{A}_n^n = \begin{bmatrix} 0 & 0 \\ \frac{v_e \tan L}{r_e \cos L} & 0 \end{bmatrix}_{2 \times 2} \quad (8)$$

$$\mathbf{A}_l^n = \begin{bmatrix} \frac{-v_n}{r_e^2} & \frac{1}{r_e} & 0 & \mathbf{0}_{1 \times 8} \\ \frac{-v_e}{r_e^2 \cos L} & 0 & \frac{1}{r_e \cos L} & \mathbf{0}_{1 \times 8} \end{bmatrix}_{2 \times 11} \quad (9)$$

$$\mathbf{A}_n^l = \begin{bmatrix} 0 & 0 \\ -v_e \left(2\omega \cos L + \frac{v_e}{r_e \cos L^2} \right) & 0 \\ 2\omega (v_n \cos L - v_d \sin L) + \frac{v_n v_e}{r_e \cos L^2} & 0 \\ 2\omega v_e \sin L & 0 \\ -\omega \sin L & 0 \\ 0 & 0 \\ -\omega \cos L - \frac{v_e}{r_e \cos L^2} & 0 \\ \mathbf{0}_{4 \times 1} & \mathbf{0}_{4 \times 1} \end{bmatrix}_{11 \times 2} \quad (10)$$

$$\mathbf{A}_l^l = \begin{bmatrix} \mathbf{N}_{7 \times 7}^l & \mathbf{D}_{7 \times 2} & \mathbf{0}_{7 \times 2} \\ \mathbf{0}_{2 \times 7} & \mathbf{B}_{2 \times 2} & \mathbf{0}_{2 \times 2} \\ \mathbf{0}_{2 \times 7} & \mathbf{0}_{2 \times 2} & \mathbf{C}_{2 \times 2} \end{bmatrix}_{11 \times 11} \quad (11)$$

where equation shown at the bottom of the next page.

where

L	latitude in radians;
r_e	Earth's radius equal to 6 378 135 m;
ω	Earth's rotation rate equal to $7.2921151467 \times 10^{-5}$ rad/s;

$f_n, f_e,$ and f_d North, East, and down specific forces;
 v_n, v_e, v_d North, East, and down velocities;
and

$$\mathbf{B} = \begin{bmatrix} \frac{-1}{\tau_b} & 0 \\ -k_3 & 0 \end{bmatrix}_{2 \times 2} \quad (12)$$

where

τ_b barometer error time constant;

k_3 barometer aiding constant used in the third-order altitude aiding feedback loop.

Additionally

$$\mathbf{D} = \begin{bmatrix} k_1 & 0 \\ \mathbf{0}_{2,1} & \mathbf{0}_{2,1} \\ -k_2 & 1 \\ \mathbf{0}_{3,1} & \mathbf{0}_{3,1} \end{bmatrix}_{7 \times 2} \quad (13)$$

where

k_1 , and k_2 are barometer aiding constants used in the third-order altitude aiding feedback loop
and

$$\mathbf{C} = \begin{bmatrix} \frac{-1}{\tau_{TV}} & 0 \\ 0 & 0 \end{bmatrix}_{2 \times 2} \quad (14)$$

where

τ_{TV} is the temporal variation bias time constant.

We now address the measurement equation for magnetic anomaly navigation. We will use the simplified measurement equation given by (3). We wish to put this measurement equation into a valid form for the MPF. From [23], the general form for the measurement equation of an MPF expresses the measurement as a sum of a nonlinear function of the nonlinear states, a linear function of the linear states, and a measurement noise w

$$\mathbf{y}_t = h_t(\mathbf{x}_t^n) + \mathbf{C}_t \mathbf{x}_t^l + w. \quad (15)$$

We slightly rearrange the measurement equation from (3) by bringing the IGRF term to the left side of the equation. Our measurement is, therefore, the raw magnetometer measurement minus the predicted IGRF field. We also break the measurement equation into a nonlinear part represented by the map interpolation function, and a linear portion that cap-

tures the temporal variation and constant bias states. The measurement equation is now

$$Z_t^m - I(\hat{\text{lat}}, \hat{\text{lon}}, \hat{\text{alt}}) = M_2(\text{lat}_{\text{ins}} + \delta\text{lat}, \text{lon}_{\text{ins}} + \delta\text{lon}) + \mathbf{C} \mathbf{x}_t^l + w \quad (16)$$

where

Z_t^m magnetometer raw measurement at time t ;

I IGRF intensity computed with an approximate position;

M_2 nonlinear 2-D interpolation function created from the 2-D map grid;

\mathbf{C} matrix representing the linear portion of the measurement equation;

w measurement noise.

The \mathbf{C} matrix shows that the measurement is also the sum of the temporal variation and constant bias states

$$\mathbf{C} = [\mathbf{0}_{1 \times 9} \ 1 \ 1]_{1 \times 11}. \quad (17)$$

Finally, we must define the measurement noise matrix and the system noise matrix. The measurement noise is modeled a zero-mean Gaussian with a variance σ_{mag}^2

$$R = E[w^2] = \sigma_{\text{mag}}^2 \quad (18)$$

where σ_{mag}^2 is the measurement accuracy for measuring the magnetic anomaly field. This is not the same thing as the magnetometer absolute accuracy, which is accurate to less than 1 nT. While the magnetometer can measure the total field to a very high accuracy, this measurement noise captures the accuracy of measuring the magnetic anomaly field, which is a single component of the total field, and therefore has a higher noise variance due to the various errors presented in the measurement equation section. The nonlinear states do not have any dynamic noise terms. The discretized nonlinear process noise v_d^n is given by

$$E[\mathbf{v}_d^n \mathbf{v}_d^{nT}] = \begin{bmatrix} 0 & 0 \\ 0 & 0 \end{bmatrix}_{2 \times 2}. \quad (19)$$

The linear-state dynamics noise captures the velocity and angular random walk of the IMU and the driving noise for the temporal variation bias. The discretized linear process

$$\mathbf{N}^l = \begin{bmatrix} 0 & 0 & 0 & -1 & 0 & 0 & 0 \\ \frac{v_e^2 \tan L - v_n v_d}{r_e^2} & \frac{v_d}{r_e} & -2\left(\omega \sin L + \frac{v_e \tan L}{r_e}\right) & \frac{v_n}{r_e} & 0 & -f_d & f_e \\ -v_e \frac{v_n \tan L + v_d}{r_e^2} & 2\omega \sin L + \frac{v_e \tan L}{r_e} & \frac{v_n \tan L + v_d}{r_e} & 2\omega \cos L + \frac{v_e}{r_e} & f_d & 0 & -f_n \\ \frac{v_n^2 + v_e^2}{r_e^2} & -2\frac{v_n}{r_e} & -2\left(\omega \cos L - \frac{v_e}{r_e}\right) & 0 & -f_e & f_n & 0 \\ \frac{-v_e^2}{r_e^2} & 0 & \frac{1}{r_e} & 0 & 0 & -\omega \sin L - \frac{v_e \tan L}{r_e} & \frac{v_n}{r_e} \\ \frac{v_n}{r_e^2} & \frac{-1}{r_e} & 0 & 0 & \omega \sin L + \frac{v_e \tan L}{r_e} & 0 & \omega \cos L + \frac{v_e}{r_e} \\ \frac{v_e \tan L}{r_e^2} & 0 & \frac{-\tan L}{r_e} & 0 & \frac{-v_n}{r_e} & -\omega \cos L - \frac{v_e}{r_e} & 0 \end{bmatrix}_{7 \times 7}$$

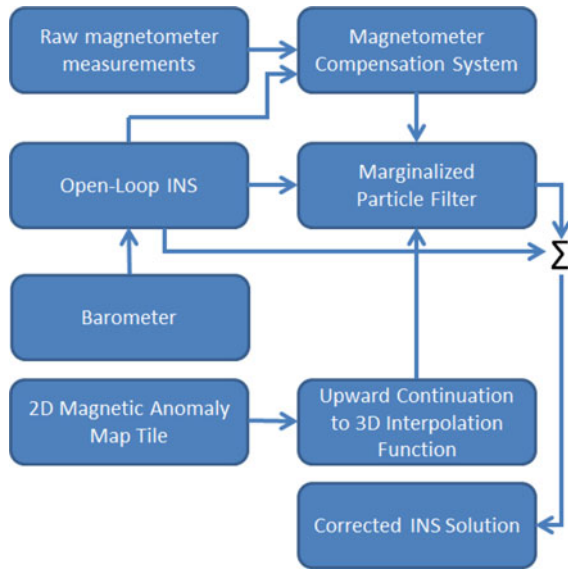


Fig. 1. Magnetic anomaly navigation flowchart.

noise v_d^l is given by

$$E[v_d^l v_d^{lT}] = \text{diag} \left(\begin{bmatrix} 0 & \mathbf{VRW}_{1 \times 3} & \mathbf{ARW}_{1 \times 3} & B & 0 & T & 0 \end{bmatrix} \right)_{11 \times 11} \quad (20)$$

$$B = \frac{2\sigma_b^2}{\tau_b} \quad (21)$$

$$T = \frac{2\sigma_{tv}^2}{\tau_{tv}} \quad (22)$$

where \mathbf{VRW} zero-mean Gaussian noise covariance of the velocity random walk;

\mathbf{ARW} zero-mean Gaussian noise covariance of the angular random walk;

B and T driving noise strengths for the barometer and temporal variation moving biases;

σ_b^2 barometer error variance;

τ_b barometer error time constant;

σ_{tv}^2 temporal variation variance;

τ_{tv} temporal variation time constant.

The filter approach can now be implemented in the MPF algorithm given in [23]. The details of this implementation are given in the Appendix. Fig. 1 shows a flowchart of the implemented filter

IV. RESULTS

A. Flight Test Data

We contracted out a flight test to a geo-survey company called Sander Geophysics to test the accuracy of the developed navigation system. Fig. 2 shows the geo-survey aircraft taking off.

The magnetometer used to generate the results in this paper is located in the lower tail boom. A magnetic anomaly map was created by Sander Geophysics over Louisa, VA, in 2012. We re-mapped a subset of this previously mapped area to evaluate map stability. We flew over the mapped area collecting data with a Geometrics 823A optically pumped



Fig. 2. Geo-survey aircraft taking off for test flight—magnetometers located on tail boom.

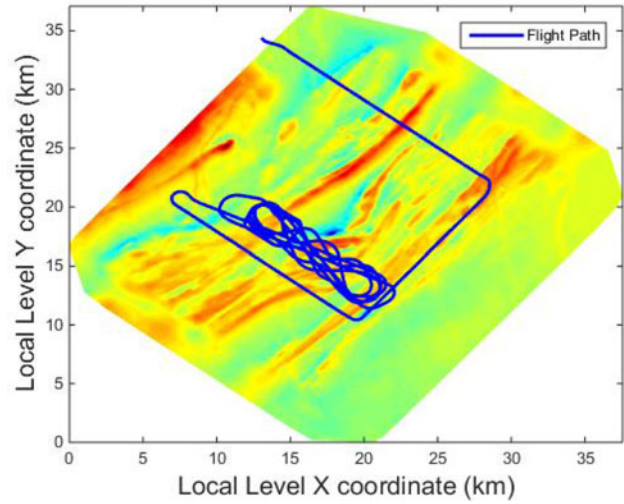


Fig. 3. 2012 magnetic anomaly map over Louisa VA and 2015 flight profile over mapped area.

cesium magnetometer, a barometer, and a navigation-grade inertial navigation system. We input this collected data and the 2012 magnetic anomaly map into our navigation filter. The magnetic anomaly map as well as the flight path is shown in Fig. 3. The magnetic anomaly map is contrast-stretched to better show the magnetic anomaly variations. The field varies from approximately -200 to 800 nT, with a standard deviation of 104 nT. The flight begins with a U-shaped trajectory covering a large area of the 2012 map followed by figure 8-s over the area we re-mapped in 2015. The gradients in the magnetic field at this altitude and at this location can be considered on the moderate to high end of what generally exists around the United States at similar altitudes. The survey area had rolling hills from approximately 75 -m MSL to 175 -m MSL, and consisted mostly of forest and farmland.

The magnetic anomaly map can be used to create an interpolation function. The expected measurement for the flight can be obtained by passing the true GPS flight position through the interpolation function. This expected measurement is not used by the filter, as it requires the use of GPS, but is only used to gain insight into how well the actual raw measurements match the magnetic anomaly map. We validate our measurement equation in Table I.

TABLE I
Measurement Equation Validation

Error term	Standard deviation of difference between predicted and measured magnetic field (nT)
No corrections	21.21 nT
IGRF correction	3.35 nT
IGRF and temporal variation correction	2.09 nT
IGRF, temporal variation, and aircraft field correction	1.55 nT

Each row of the table removes an additional source of error from the raw measurements. The standard deviation of the difference between the expected measurements and the actual measurements is then given. The standard deviation decreases sharply with the removal of the IGRF field. The temporal variations are removed by subtracting the measured variations of a nearby base station, which was within 5–10 km of the aircraft. These base station data are not assumed available while flying, but is shown here to help validate the measurement equation. A slight decrease in the standard deviation of the expected and actual measurements is observed when the temporal variations are removed. Finally, the effects of the aircraft field are removed with an aircraft-field compensation system. These compensated measurements were provided by Sander Geophysics and are computed by applying compensation coefficients obtained during a calibration flight to the remaining flight data. The lowest standard deviation of the difference between the expected measurements and the actual measurements is obtained after applying this final correction. The final standard deviation of the error between the expected and actual measurements is 1.55 nT, roughly 1% of the total variation seen in the magnetic intensity along the flight profile. This is analogous to a high signal-to-noise ratio, and provides valuable insight into expected navigation performance. Fig. 4 shows a 6-min segment of the errors between the expected measurement and the raw magnetometer measurements with all of the previously described errors removed. As can be seen in the figure, the errors are time correlated with a time constant on the order of less than a minute. We believe these remaining errors are the result of using an under-sampled map, although a test flight using a fully sampled map would be necessary to determine if this is truly the case. If this is the case, then using a fully sampled map should lead to higher navigation accuracy, as we believe these errors are the dominant errors remaining in the measurements.

B. Map Stability

In addition to collecting data to test the navigation system, we flew a magnetic survey over a subset of the original 2012 survey area. The resulting map was almost identical to the previous map. We computed the difference between the two maps, as shown in Fig. 5. Both maps, with the exception of the edges, have a max difference of around

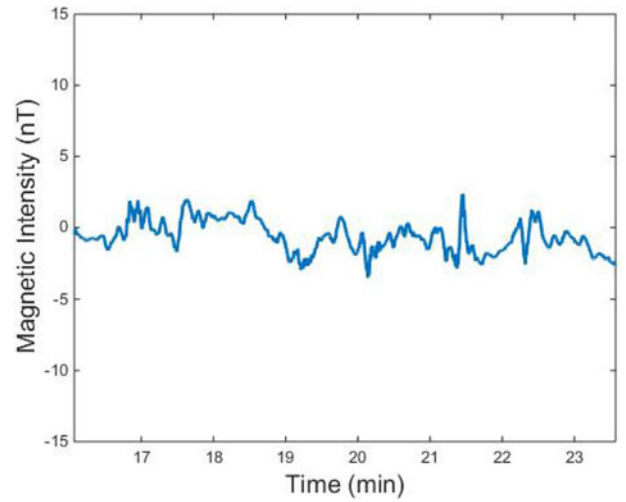


Fig. 4. Difference between the expected measurements from interpolation function (using true GPS positions) and the raw measurements (made zero-mean).

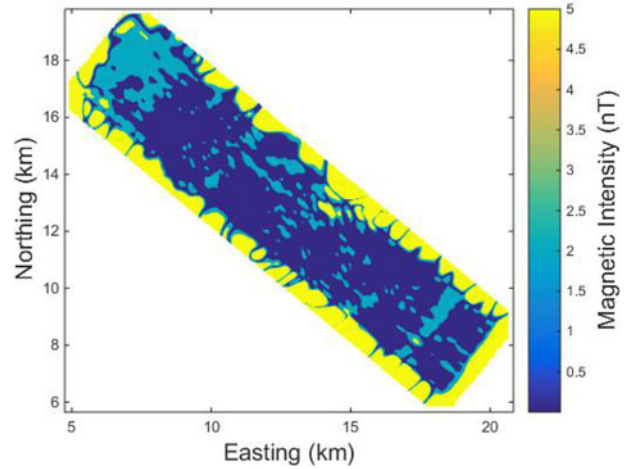


Fig. 5. Difference between the 2012 magnetic anomaly map and the 2015 magnetic anomaly map.

2 nT. The errors on the edges of the map are an artifact of how the maps were processed—a larger map would push these errors out further. When ignoring the edge effects, the standard deviation of the error between the two maps is 1.2 nT. This gives further evidence that the magnetic anomaly maps are stable over time, or at least will not be a driving error term in a navigation filter. These errors would appear as slowly varying biases on the order of a single nT—the previously shown errors vary much quicker than this, and by a larger amount, so map stability does not appear to be a driving error term for navigation accuracy.

C. Navigation Results

We ran the designed navigation filter using the collected flight data combined with the 2012 survey map. We assume the navigation filter starts with GPS-level position uncertainty to simulate a sudden loss in GPS, at which time an alternative navigation system must be used. We also tested a “cold-start” case in which the filter begins with a much

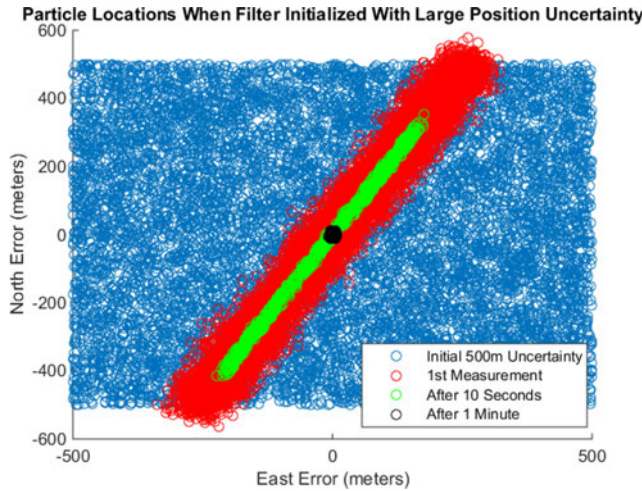


Fig. 6. Demonstration of filter “cold-start” with large initial position uncertainty.

TABLE II
Navigation Accuracy Results

	North channel	East channel
Mean	-2.2 m	2.7 m
Standard deviation	9.0 m	8.9 m
DRMS	13.1 m	
Unaided INS error after 1 h	344 m	

larger uncertainty. In this case, the filter is able to converge to a unimodal solution after approximately 1 min, as shown in Fig. 6. The navigation filter processed an hour of data in approximately 10 min using MATLAB, a high-level programming language. This indicates that computation is low enough to easily allow for real time use. Storage requirements for the magnetic anomaly maps are also fairly small—we were only using a small regional map tile, but a map of the entire United States at one altitude was only 30 MB. This size will increase when upward continuing the data but will still be on the order of mega-bytes, not giga-bytes.

The INS mechanization was run independently of the rest of the filter, with barometer aiding occurring in the mechanization equations. No feedback was provided by the filter, although feedback may be required with a less accurate INS. In our flight test, the INS did not drift far enough to benefit from loop closure. The INS provided the reference trajectory for the filter, which estimated the errors in the INS. The INS solution is used while evaluating the map interpolation function, as shown in (16), as well as when computing the dynamics matrix, which depends on latitude, velocity, and specific forces. We ran the filter against an hour long segment of the flight profile using only INS, barometer, and magnetometer measurements. We then used the true GPS solution to evaluate the performance of the filter. Fig. 7 shows the North and East errors over the hour long flight as well as the predicted filter standard deviations. The statistics for the flight are given in Table II. Overall, the system obtained a DRMS error of 13 m. The

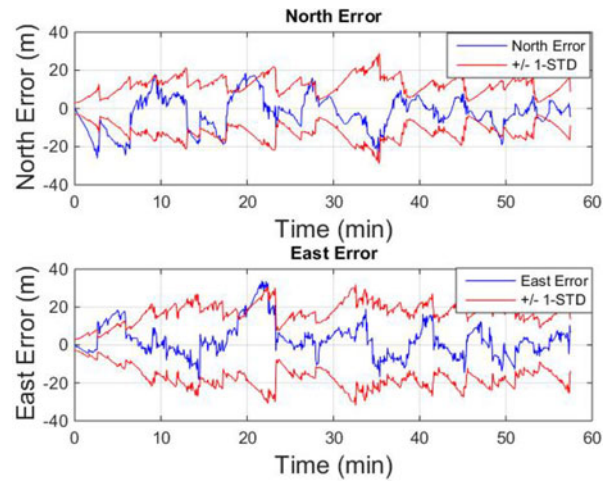


Fig. 7. North and East error over 1-h segment of flight profile.

filter clearly constrained the drift of the INS. Furthermore, the filter’s covariance bounds appear reasonable. It is important to note that the filter’s covariance bounds are strongly correlated with the gradient of the magnetic field at a given location. Steeper magnetic gradients lead to a more accurate position estimate, and shallower gradients lead to a degraded position estimate. The navigation-grade INS provides an excellent short term solution to help the navigation solution pass through these areas of low magnetic gradient without losing too much accuracy. A high quality (navigation grade) INS is important to achieving the accuracies we have demonstrated here. It is also apparent that the filter standard deviation has reached a steady-state that varies around 10–20 m. The mean error in the North and East channels are both less than 3 m, and the plots indicate it is reasonable to consider the errors zero-mean, with no clear bias existing in the North or East channels. The standard deviations of the North and East channels are very similar. This is expected due to the fact that the steep gradients that exist in the map are in a North-East to South-West direction. Flying over a different area may have better or worse errors in one channel due to consistently steeper North or East gradients. Due to the accurate modeling of the INS, the corrected latitude and longitude errors also lead to corrected velocity errors of approximately 0.1 m/s. The use of a navigation grade INS for these results was useful but not absolutely required. Lower grade INS may be used with a magnetic anomaly navigation system but overall filter performance should be expected to decrease. Looking at the sawtooth shape of the position covariance in Fig. 7, it is clear there are areas where the covariance starts to grow quickly. These areas correspond very closely with areas of shallow magnetic gradient on the map. A lower grade INS would have a solution that grew much more quickly in these areas. The same saw tooth covariance would be observed, however, the variation would be much greater. An INS that drifted too quickly could cause the particle filter to begin to find incorrect areas on the map and give multimodal position estimates, possibly leading to filter divergence. The use of a tactical grade INS has been previously tested in simu-

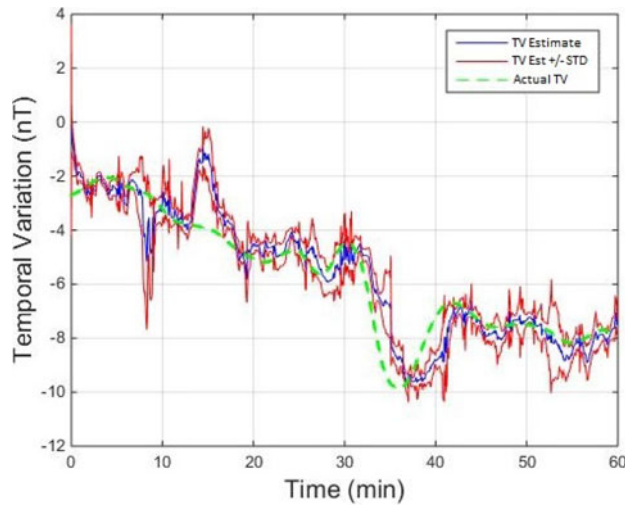


Fig. 8. Filter estimation of temporal variations.

lation by the authors and seems feasible but anything worse will likely lead to filter divergence. Additionally, it is useful to compare the navigation accuracy during the first portion of the flight test with the second portion. The first portion consisted of flying a “U” shape trajectory with each leg of the “U” approximately 20 km. This segment of the flight test had much lower dynamics than the remaining portion of the flight test, which consisted of large figure-8 turns. There are no significant changes in navigation accuracy between these two flight segments. In general, high platform dynamics will increase navigation accuracy but the spatial variation at low altitudes is sufficient to lead to an accurate navigation solution regardless of platform dynamics. When flying at higher altitudes platform dynamics may become a more important variable. Finally, it is important to note the sharp drops in the filter’s covariance as seen in Fig. 7. These drops in covariance correlate with sudden changes in the magnetic anomaly field gradient. When the gradient changes quickly in both the North and East directions, such as occurs when flying over “bump” or “bowl” in the magnetic anomaly map, the covariance can quickly collapse in both directions.

The filter also estimated the temporal variations. The temporal variations were rather calm on the day of the flight, so in order to better determine the filter observability of these variations we further artificially corrupted the measurements with actual recorded data from a different magnetically stormy day in a second filter run. Previously shown in Fig. 4, even with the temporal variations removed, the measurements have remaining high frequency errors with a standard deviation of around 2 nT. Consequently, the filter is only able to estimate the larger, longer wavelength (therefore, lower frequency) components of the temporal variations. Fig. 8 shows the filter’s estimation of the temporal variations on the stormy day. When the magnetometer measurements were corrupted to simulate the stormy day, the filter achieved a DRMS error of 15 m—only a mild increase in errors compared to a DRMS of 13.1 m on the quiet day. It is important to note that the filter temporal variation state is estimating *any* residual error in the measurements, so it

will not match the actual temporal variations exactly. The temporal variation state is also capturing any residual aircraft fields, variations from the map altitude, or uncaptured high frequency crustal components (the 2012 map was not quite fully sampled). The apparent lag in the estimation of the temporal variations is caused by the tuning parameters related to the temporal variation state. Better filter performance was achieved when using a long time constant for the temporal variation state. Restricting the temporal variation state to slow changes increases filter stability. If a short time constant was used for the temporal variations, the filter began to assume most of the changes in the measurements were due to changing temporal variations, which degraded filter performance. A bad magnetic storm in the context of magnetic anomaly navigation does not so much correspond to large temporal variations as it does to large higher frequency variations. A magnetic storm could cause a large rise in the magnetic field, but if this change is slow relative to how the crustal field is changing throughout the flight, the filter will likely retain observability of the temporal variations. Temporal variations or aircraft fields with frequencies that overlap with the crustal field frequencies are much more problematic for a navigation filter than slowly varying errors. Conversely, temporal variations and aircraft field frequencies that are much higher than the crustal field frequencies tend to average out, and do not greatly degrade navigation performance.

V. CONCLUSION

The presented navigation filter achieved DRMS errors of around 13 m under favorable conditions with actual flight test data. These conditions included a relatively low altitude, a high quality magnetic anomaly map, and a clean sensor environment. The accuracy results achieved in this paper are orders of magnitude better than previously published flight test results using magnetic anomaly maps and magnetometers. This is primarily due to the scalar high sensitivity optically pumped magnetometers that were used rather than less accurate currently available vector magnetometers. The accuracies demonstrated in this paper using only passive sensors demonstrate that navigation using the Earth’s magnetic anomaly field may be a viable approach for future GPS backup and alternative systems for aircraft in flight.

APPENDIX

MAGNETIC NAVIGATION ALGORITHM

In this section, we present the filter algorithm that is needed to implement the previously described magnetic anomaly navigation system. This algorithm follows closely from the MPF algorithm given in [23], with added detail on the map precomputation steps as well as how the INS reference trajectory is used. Recall that each particle has an associated Kalman filter. Because there are only nonlinearities in the measurement equation, and not in the state dynamics, many of the Kalman filter equations can be evaluated once for all particles [23].

Algorithm 1: Magnetic Anomaly Marginalized Particle Filter Algorithm.

Algorithm Input: Magnetic anomaly map, raw magnetometer measurements, INS ΔV 's and $\Delta \Theta$'s, barometer-derived altitude, IGRF model

Algorithm Output: Errors in an INS navigation solution including position errors, velocity errors, and tilt errors

Notation: (i) denotes an individual particle, **bold** denotes vectors and matrices, superscripts l and n denote the linear and nonlinear states, respectively, and t denotes current time step, and $t - \Delta t$ denotes the previous time step.

1) Initialization:

a) Create interpolation function $M_2 = f(\text{lat}, \text{lon})$ from magnetic anomaly grid. Choose number of particles equal to N .

b) For $i = 1, \dots, N$ initialize the nonlinear particles by drawing from a Gaussian distribution with mean μ_0^n and covariance P_0^n : $\mathbf{x}_0^{n,(i)} \sim \mathcal{N}(\mu_0^n, P_0^n)$. Next, initialize all the linear state particles with the same initial conditions: $\mathbf{x}_0^{l,(i)} = \bar{\mathbf{x}}_0^l$. Finally, initialize the linear particle covariance, which is a single common matrix for all of the linear particles, as $\mathbf{P}_0 = \bar{\mathbf{P}}_0$

2) INS Mechanization: Use the new ΔV 's and $\Delta \Theta$ measurements to compute the INS solution at time t . Barometer aiding occurs at this step.

3) Compute Dynamics Matrix: Use the INS solution to compute \mathbf{A}_t^n , \mathbf{A}_t^l , \mathbf{A}_t^n , and \mathbf{A}_t^l at time t .

4) Evaluate IGRF Model: Use the filter estimated position, given as INS + $\hat{\mathbf{x}}$, to evaluate the IGRF model for the filter estimated latitude, longitude, and altitude.

5) Particle Filter Measurement Update: For $i = 1, \dots, N$

a) Evaluate the expected magnetic intensity for each particle hypothesis. The expected intensity is based on both the particle's location hypothesis (nonlinear states 1 and 2) and the temporal variation hypothesis (linear state 8)

$$I_t^{(i)} = M_2(\text{lat}_t^{\text{ins}} + x_t^{n,(i)}(1), \text{lon}_t^{\text{ins}} + x_t^{n,(i)}(2)) + x_t^{l,(i)}(8). \quad (23)$$

Using the raw magnetometer measurement y_t denote the residual particle intensity by $e_t^{(i)} = y_t - (I_t^{(i)} + \text{IGRF})$.

b) The measurements are assumed Gaussian with mean $e_t^{(i)}$ and covariance $V_t = \mathbf{C}\mathbf{P}_{t|t-\Delta t}\mathbf{C}^T + R$. \mathbf{C} is the linear measurement matrix, in this case $[\mathbf{0}_{1 \times 9}, 1, 1]_{1 \times 11}$, and $\mathbf{P}_{t|t-\Delta t}$ is the linear state's Kalman filter covariance. We can evaluate the probability for each particle from a Gaussian distribution given by

$$q_t^{(i)} = \exp\left(-\frac{1}{2}\left(e_t^{(i)}V_t^{-1}e_t^{(i)T}\right)\right). \quad (24)$$

The weights then must be normalized according to

$$\tilde{q}_t^{(i)} = \frac{q_t^{(i)}}{\sum_{j=1}^N q_t^{(j)}}. \quad (25)$$

6) Resampling: Resample particles with a chosen resampling strategy. We resampled at each step with sequential importance sampling [25].

7) Kalman Filter Measurement Update: The next step is to update the linear states of the Kalman Filter with the measurement. We first define the Kalman gain matrix and covariance matrix, which are the same for all particles

$$\mathbf{K}_t = \mathbf{P}_{t|t-\Delta t}\mathbf{C}^T V_t^{-1} \quad (26)$$

$$\mathbf{P}_{t|t} = \mathbf{P}_{t|t-\Delta t} - \mathbf{K}_t V_t \mathbf{K}_t^T. \quad (27)$$

We next calculate a measurement residual $J_t^{(i)}$ and apply the Kalman gain for each individual particle to determine the Kalman filter updated linear state.

For $i = 1, \dots, N$

$$J_t^{(i)} = M_2(\text{lat}_t^{\text{ins}} + \mathbf{x}_t^{n,(i)}(1), \text{lon}_t^{\text{ins}} + \mathbf{x}_t^{n,(i)}(2)) + \mathbf{x}_t^{l,(i)}(8) \quad (28)$$

$$\hat{\mathbf{x}}_{t|t}^{l,(i)} = \hat{\mathbf{x}}_{t|t-\Delta t}^{l,(i)} + \mathbf{K}_t \left(y_t - J_t^{(i)}\right). \quad (29)$$

8) Particle Filter Time Update: The particles are propagated in time according to the system dynamics model. First, compute the Cholesky decomposition $\mathbf{q}_{\text{chol}} = \text{chol}\left(\mathbf{A}_t^n \mathbf{P}_{t|t} (\mathbf{A}_t^n)^T + \mathbf{Q}^n\right)$. Random noise must be added to the nonlinear states, which is denoted by a function randn to represent adding white Gaussian noise. The particles are then propagated according to

$$\mathbf{x}_{t+1}^{n,(i)} = \mathbf{A}_t^n \mathbf{x}_{t|t}^{n,(i)} + \mathbf{A}_t^n \mathbf{x}_{t|t}^{l,(i)} + \mathbf{q}_{\text{chol}} \cdot \text{randn}(2 \times 1) \quad (30)$$

9) Kalman Filter Time Update: Define two intermediate matrices, N_t and L_t , which are the same for each particle, and compute the propagated Kalman filter covariance, which is also the same for each particle

$$\mathbf{N}_t = \mathbf{A}_t^n \mathbf{P}_{t|t} (\mathbf{A}_t^n)^T + \mathbf{Q}^n \quad (31)$$

$$\mathbf{L}_t = \mathbf{A}_t^l \mathbf{P}_{t|t} \mathbf{A}_t^{lT} \mathbf{N}_t^{-1} \quad (32)$$

$$\mathbf{P}_{t+1|t} = \mathbf{A}_t^l \mathbf{P}_{t|t} (\mathbf{A}_t^l)^T + \mathbf{Q}^l - \mathbf{L}_t \mathbf{N}_t \mathbf{L}_t^T. \quad (33)$$

Finally, define a time update residual for each particle and calculate the time update. For $i = 1, \dots, N$

$$\mathbf{z}_t^{(i)} = \mathbf{x}_{t+1|t}^{n,(i)} - \mathbf{A}_t^n \mathbf{x}_{t|t}^{n,(i)} \quad (34)$$

$$\mathbf{x}_{t+1|t}^{l,(i)} = \mathbf{A}_t^l \mathbf{x}_{t|t}^{l,(i)} + \mathbf{A}_t^n \mathbf{x}_{t|t}^{n,(i)} + \mathbf{L}_t (\mathbf{z}_t^{(i)} - \mathbf{A}_t^n \mathbf{x}_{t|t}^{l,(i)}). \quad (35)$$

10) Determine the expected means and covariances of the nonlinear and linear states. The covariance of the linear states is already computed as $\mathbf{P}_{t+1|t}$

$$\hat{\mathbf{x}}_{t|t}^l = \sum_{i=1}^N \hat{q}_t^{(i)} \hat{\mathbf{x}}_{t|t}^{l,(i)} \quad (36)$$

$$\hat{\mathbf{x}}_{t|t}^n = \sum_{i=1}^N \hat{q}_t^{(i)} \hat{\mathbf{x}}_{t|t}^{n,(i)} \quad (37)$$

$$\hat{\mathbf{P}}_{t|t}^n = \sum_{i=1}^N \hat{q}_t^{(i)} \left(\left(\hat{\mathbf{x}}_{t|t}^{n,(i)} - \hat{\mathbf{x}}_{t|t}^n \right) \left(\hat{\mathbf{x}}_{t|t}^{n,(i)} - \hat{\mathbf{x}}_{t|t}^n \right)^T \right). \quad (38)$$

- 11) Move to the next measurement time t and iterate from step 2.

ACKNOWLEDGMENT

The authors would like to thank Dr. R. Lutwak at DARPA for providing the funds needed to conduct this research.

Disclaimer: The views expressed in this paper are those of the authors, and do not reflect the official policy or positions of the United States Air Force, Department of Defense, or U.S. Government.

REFERENCES

- [1] J. Hollowell
Heli/SITAN: A terrain referenced navigation algorithm for helicopters
In *Proc. IEEE Symp. Position Location Navigat.*, Mar. 1990, pp. 616–625.
- [2] A. DeGregoria
Gravity gradiometry and map matching: An aid to aircraft inertial navigation systems Thesis, Air Force Inst. Technol., Fairborn, OH, USA, 2010.
- [3] B. Sinopoli, M. Micheli, G. Donato, and T. Koo
Vision based navigation for an unmanned aerial vehicle
In *Proc. 2001 ICRA. IEEE Int. Conf. Robot. Autom.*, 2001, pp. 1757–1764.
- [4] J. A. Schockley
Ground vehicle navigation using magnetic field variation
Dissertation, Air Force Inst. Technol., Fairborn, OH, USA, 2012.
- [5] W. Storms, J. Shockley, and J. Raquet
Magnetic field navigation in an indoor environment
In *Proc. Ubiquitous Positioning Indoor Navigat. Location Based Service*, 2010, pp. 1–10.
- [6] A. B. Reid
Aeromagnetic survey design
Geophysics, vol. 45, no. 5, pp. 937–976, 1980.
- [7] C. Dahlgren
Non-linear black box modeling of JAS 39 Gripen's radar altimeter Master's thesis
LiTH-ISY-EX-1958, Dept. E.E., Linköping University, Linköping, Sweden, 1998.
- [8] W. J. Hinze, R. Von Frese, and A. H. Saad
Gravity and Magnetic Exploration: Principles, Practices, and Applications. Cambridge, U.K.: Cambridge Univ. Press, 1998.
- [9] R. A. Langel and W. J. Hinze
The Magnetic Field of the Earth's Lithosphere: The Satellite Perspective. Cambridge, U.K.: Cambridge Univ. Press, 1998.
- [10] A. Canciani and J. Raquet
Absolute positioning using the Earth's magnetic anomaly field
In *Proc. Int. Tech. Meeting Inst. Navigat.*, 2015, pp. 265–278.
- [11] V. Bankey *et al.*,
Digital data grids for the magnetic anomaly map of North America: U.S. geological survey open-file report 02-414
U.S. Geological Survey, Denver, CO, USA, 2002.
- [12] R. J. Blakely
Potential Theory in Gravity and Magnetic Applications. Cambridge, U.K.: Cambridge Univ. Press, 1996.
- [13] N. Bergman
Point-mass filter and Cramer-Rao bound for terrain-aided navigation
In *Proc. 36th IEEE Conf. Decision Control*, 1997, pp. 565–570.
- [14] M. B. May and P. D. Meisin
Testing of the geomagnetic navigation concept
Naval Command, Control Ocean Surveillance Center, 1989.
- [15] M. L. Psiaki, S. M. Fox, and L. Huang
Ground tests of magnetometer-based autonomous navigation (MAGNAV) for low-earth-orbiting spacecraft
J. Guid., Control, Dyn., vol. 16, no. 1, pp. 206–214, 1993.
- [16] J. M. Wilson and R. J. Kline-Schoder
Passive navigation using local magnetic field variations
In *Proc. Nat. Tech. Meeting Inst. Navigat.*, 2006, pp. 770–779.
- [17] P. Hood
History of aeromagnetic surveying in Canada
Leading Edge, vol. 26, no. 11, pp. 1384–1392, 2007.
- [18] Xu, Y. Zun, L. Yi, and Y. Lei
A new correlation matching algorithm based on differential evolution of geomagnetic aid navigation
Appl. Mech. Mater., vol. 2032, no. 038, pp. 94–96, 2011.
- [19] L. Ming-Ming, H.-Q. Lu, H. Yin, and X.-L. Luang
Novel algorithm for geomagnetic navigation
J. Central South Univ. Technol., vol. 18, pp. 791–799, 2011.
- [20] C. Guo, L. Anliang, H. Cai, and Y. Huabo
Algorithm for geomagnetic navigation and its validity evaluation
In *Proc. IEEE Int. Conf. Comput. Sci. Autom. Eng.*, 2011, pp. 573–577.
- [21] F. Goldenberg
Geomagnetic navigation beyond the magnetic compass
In *Proc. IEEE/ION Position, Location, Navigat. Symp.*, 2006, pp. 684–694.
- [22] D. Budker
Optical Magnetometry. Cambridge, U.K.: Cambridge Univ. Press, 2013.
- [23] T. Schon, F. Gustafsson, and P.-J. Nordland
Marginalized particle filters for mixed linear/nonlinear state-space models
IEEE Trans. Signal Process., vol. 53, no. 7, pp. 2279–2289, Jul. 2005.
- [24] D. Titterton and J. L. Weston
Strapdown Inertial Navigation Technology. London, U.K.: Peter Peregrinus Ltd., 1997.
- [25] J. S. Liu, R. Chen, and T. Logvinenko
A theoretical framework for sequential importance sampling with resampling
In *Sequential Monte Carlo Methods in Practice*. New York, NY, USA: Springer-Verlag, 2001, pp. 225–246.

Aaron Canciani received the Bachelor's of Science degree in electrical engineering from the US Air Force Academy, CO, USA, and the Master's of Science degree in electrical engineering from Air Force Institute of Technology (AFIT), Fairborn, OH, USA. He is currently working toward the Ph.D. degree at the AFIT.

He is currently with AFIT's Autonomy and Navigation Technology Center, where he researches alternative navigation systems.

John Raquet is currently the Director of the Autonomy and Navigation Technology Center, Air Force Institute of Technology, Fairborn, OH, USA, where he is also a Professor of electrical engineering. He has been involved in navigation research for more than 25 years.